JOURNAL OF PROPULSION AND POWER
Vol. 18, No. 6, November–December 2002

Experimental Study of the Transient Underexpanded Jet Generated by Electrothermal Capillary Plasma

Jong-Uk Kim,* N. T. Clemens,† and P. L. Varghese‡
University of Texas at Austin, Austin, Texas 78712-1085

An investigation has been conducted of the characteristics of a highly underexpanded pulsed plasma jet originating from a 3.1-kJ electrothermal capillary discharge. Excitation temperatures and electron number densities were derived from spatially and temporally resolved emission spectra, and the flowfield was visualized using laser schlieren imaging. The emission measurements were made at several locations along the jet axis and at several times during the course of the discharge, to investigate the development of the jet temperature and electron density fields. In general, it is found that the temperature and electron density axial profiles are similar when the axial location is normalized by the distance from the jet exit to the Mach disk. For most of the discharge, the excitation temperatures upstream of the Mach disk are about 1 eV (12,000 K), but increase to 1.7 eV (20,000 K) just downstream of the Mach disk. Similarly, the electron number densities are of order 10^{17} and 10^{18} cm^{-3}, for locations upstream and downstream of the Mach disk, respectively. Analysis of the trajectory of the blast wave shows that it is best modeled by accounting for continuous, rather than instantaneous, deposition of energy at a point.

Nomenclature

A_{ul}	=	spontaneous emission rate from upper to lower states
C	=	capacitance
D	=	capillary bore exit diameter
E	=	total energy deposited
E_s	=	electrical energy stored in the capacitor
E_u	=	energy of the excited state
$g_{u,l}$	=	statistical weight factor
I	=	intensity of an emission line
i	=	current in pulse forming network
k	=	Boltzmann's constant
L	=	optical path length
L_{eff}	=	effective optical path length for self-absorption
M	=	Mach number
n_e	=	electron number density
n_l	=	lower state number density
n_0	=	ground state number density
R	=	radius of the shock wave
S_{lu}	=	integrated line strength
T_{exc}	=	excitation temperature
t	=	time
U	=	shock velocity
V	=	voltage across the capacitor
V_c	=	voltage difference across the capillary
x	=	axial distance from the exit bore
$x_m(t)$	=	Mach disk location
β	=	parameter related to the rate of energy deposition
$\Delta\varepsilon_{ul}$	=	energy difference between upper and lower states
δ	=	standard deviation of a sample
ζ_t	=	nondimensional axial distance, x/x_m
λ	=	wavelength of light
μ	=	atom–ion reduced mass
ν	=	frequency of light
ρ_0	=	ambient density
τ	=	transmissivity
ϕ	=	line shape function

Presented as Paper 99-0452 at the AIAA 37th Aerospace Sciences Meeting and Exhibit, Reno, NV, 11–14 January 1999; received 10 July 1999; revision received 31 May 2002; accepted for publication 31 May 2002.

*Postdoctoral Fellow, Center for Aeromechanics Research, Department of Aerospace Engineering and Engineering Mechanics. Member AIAA.

†Associate Professor, Center for Aeromechanics Research, Department of Aerospace Engineering and Engineering Mechanics. Senior Member AIAA.

‡Professor, Center for Aeromechanics Research, Department of Aerospace Engineering and Engineering Mechanics. Senior Member AIAA.

I. Introduction

ELECTROTHERMAL (ET) plasmas are of interest for many applications, including electrothermal-chemical (ETC) guns, hypersonic mass acceleration, and spacecraft propulsion. ET plasmas are formed by electrically heating a gas, usually with a high-voltage discharge across an ablative solid, and are characterized by relatively low temperatures and high number densities. ETC gun propulsion uses a pulsed power system to generate a plasma, which is then injected into a chemical propellant to improve gun performance.[1–4] In many proposed ETC gun systems, the primary use of the plasma is to ignite a solid propellant charge; however, despite the demonstrated improvements in gun performance using ETC ignition, little is currently known about the fundamental processes of plasma-initiated combustion, or even of the characteristics of the ET plasma itself. In spacecraft propulsion, ET plasmas are used in pulsed thrusters that can achieve higher exhaust velocities than are possible with chemical rockets.[5]

The primary objective of the current work is to investigate the characteristics of capillary plasmas that are of specific interest for ETC gun applications. Previous related studies, which have used either polyethylene or polycarbonate capillaries, have investigated the characteristics of transient plasmas (typically with a duration of less than 1 ms) that are formed with supply energies ranging from 1 to 100 kJ. High-speed imaging of the plasma jet expanding into atmospheric pressure showed that it exhibits a barrel shock structure and a highly luminous region downstream of the Mach disk.[6–8] Although the details of these previous studies vary, plasma temperatures inferred from emission spectroscopy of electronic transitions of atoms and ions are not very consistent. The range of plasma temperatures reported is from about 10,000 to 50,000 K (Refs. 7 and 9–11). Electron number densities inferred from the Stark broadening of the hydrogen emission lines show better agreement because published values range from 10^{16}–10^{17} cm^{-3} (see Refs. 7 and 12).

In the present study, temporally resolved schlieren imaging and temporally and spatially resolved emission spectroscopy were used

Table 1 Spectroscopic constants[29] and absorption parameters of atomic copper lines

λ, nm	g_u	E_u, eV	g_l	E_l, eV	A_{ul}, 10^8 s^{-1}	S_{lu}, m$^2 \cdot$ Hz	n_l, m^{-3}	$S_{lu}\phi(\nu_0)n_l L_{eff}$	$\tau(\nu_0)$
510.55	4	3.816	6	1.389	0.020	9.35×10^{-9}	1.5×10^{20}	0.0078	0.99
515.32	4	6.190	2	3.785	0.60	8.53×10^{-7}	1.6×10^{19}	0.0779	0.93
521.82	6	6.191	4	3.816	0.75	8.14×10^{-7}	3.1×10^{19}	0.1467	0.86
529.25	8	7.735	8	5.394	0.109	8.05×10^{-8}	3.0×10^{19}	0.0139	0.99
570.02	4	3.816	4	1.642	0.0024	1.97×10^{-9}	8.6×10^{19}	0.0010	1.00
578.21	2	3.785	4	1.642	0.0165	6.92×10^{-9}	8.6×10^{19}	0.0034	1.00

to investigate the evolution of the structure of the plasma jet flowfield and to determine its composition, temperature, and electron density. This is a continuation of the work reported by Kohel et al.,[7] where preliminary emission spectroscopic measurements were made for a limited range of conditions.

II. Background

A. Excitation Temperature and Electron Densities of the Plasma

We use Boltzmann plots to determine excitation temperature (see Ref. 13). If the relative intensities of the spectral lines of a given species are measured, the associated excitation temperature T_{exc} can be determined from

$$\ln(I\lambda/A_{ul}g_u) = B - E_u/kT_{exc} \tag{1}$$

where I is the relative intensity of an emission line, λ is the emission wavelength, A is the spontaneous emission rate, and g_u is the degeneracy or statistical weight factor for the excited state. For a gas or plasma in local thermodynamic equilibrium (LTE), a plot of the logarithmic term on the left-hand side vs the excited state energy E_u should yield a straight line with slope $-1/kT_{exc}$. Emission resulting from several electronic transitions of neutral atomic copper was observed in the spectral regions between 465 and 585 nm. The six atomic copper lines used in the analysis and their spectroscopic constants are listed in Table 1. (Note that in Ref. 7, the incorrect degeneracy of the upper state of the 529.25-nm line was used, which resulted in all of the temperatures reported in that paper being about 15% too high.) The distinct atomic lines observed in emission are reasonably well represented by a Lorentzian line shape. This is because Stark broadening, which arises from perturbations of the atomic system by electrons and ions, is the dominant broadening mechanism at the temperatures and electron number densities encountered in this study (see Refs. 14–17).

The emission spectra can also be used to infer the electron number density because Stark-broadened linewidths are directly related to electron density. Because the Stark effect is well-characterized in hydrogen, and the transitions fall within a convenient region of the optical spectrum, the Balmer series was used for the line-shape analysis (see Ref. 15). The most frequently measured Balmer line is H_β (486.1 nm), which occupies a very convenient region of the spectrum, has a rather characteristic and broad profile, and is far less sensitive to radiative transfer effects than H_α (656.3 nm) (Ref. 15). In the plasmas studied in this work, however, measurement of the H_β linewidth is complicated by overlap with adjacent emission lines from other species. Thus, our line-shape analysis focuses on the more prominent H_α line. Widths for the observed H_α lines are determined by a nonlinear least-squares fit of the recorded line shapes to a Lorentzian function. Instrumental broadening for our system is reasonably well characterized by a Lorentzian, with a full-width-at-half-maximum (FWHM) of 0.62 nm. Because the convolution of two Lorentzian profiles yields another Lorentzian whose width is the sum of the two component profiles, the instrumental broadening is simply subtracted from the measured FWHM values to obtain the true Stark-broadened widths.

B. Plasma Jet Structure

The plasma jet ejected from the open end of the capillary forms a highly underexpanded jet with a characteristic barrel shock structure. In a previous study[7] time-resolved visible emission images

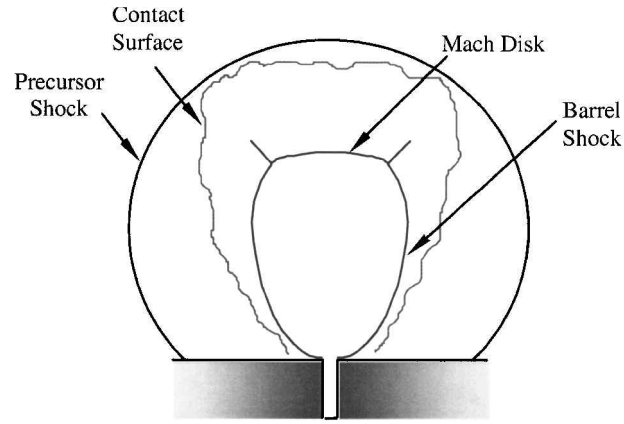

Fig. 1a Principal features of a transient underexpanded free jet.

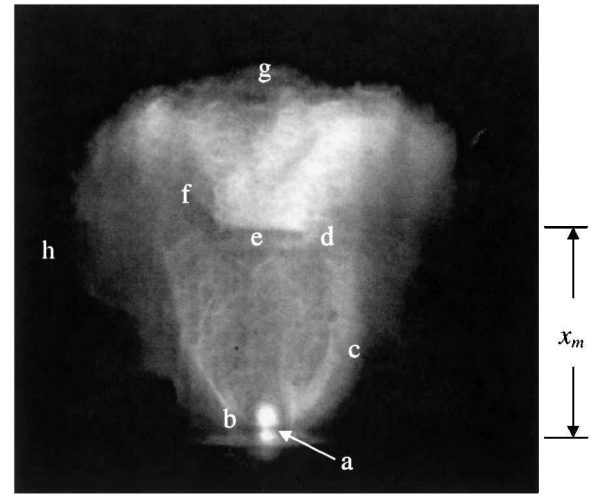

Fig. 1b Short duration (250 ns) image of plasma jet emission: a) bore exit, b) Prandtl–Meyer expansion (Mach cone), c) barrel shock, d) triple point, e) Mach disk, f) reflected shock, g) contact surface, and h) jet boundary, respectively; x_m is the Mach disk location (from Ref. 18).

of the plasma jet were obtained using a gated intensified charge-coupled device (ICCD) detector. A similar type of image, taken about 95 μs after the initiation of the discharge, is shown in Fig. 1 (see Ref. 18), together with a schematic description of notable features of the transient underexpanded jet flow. Expansion waves at the bore exit travel to the jet boundary where they are reflected to form weak compression waves that coalesce into the barrel shock. The barrel shock undergoes an irregular reflection and, in the triple-point downstream from the exit bore, the reflected shock, Mach disk, and slip surface are formed.[19–22] In the shock-bounded, highly underexpanded jet flow region, the flow is characterized by relatively high Mach numbers ($M \gg 1$), low pressures, and low temperatures. Across the Mach disk, the flow is decelerated to subsonic velocity, the pressure rises suddenly to atmospheric pressure or above, and the temperature increases due to shock heating by the Mach disk.[19–22]

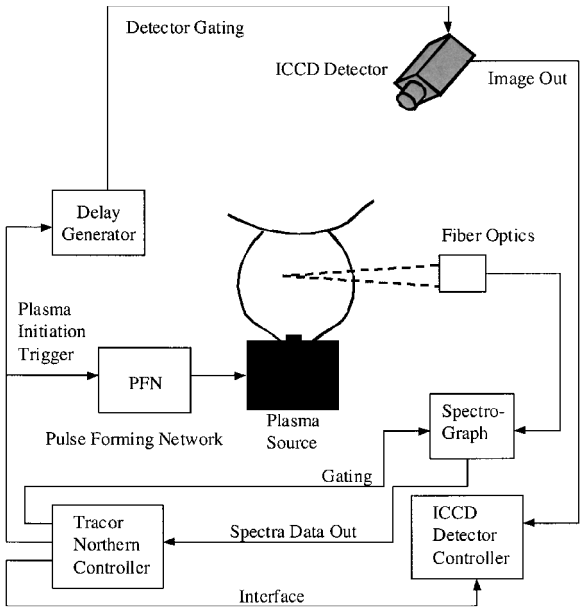

Fig. 2 Schematic diagram of the experimental setup for acquiring emission images and temporally and spatially resolved spectra of the plasma jet.

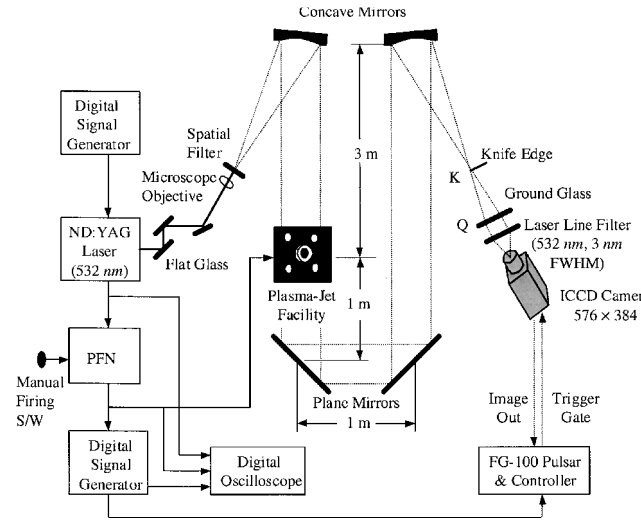

Fig. 3 Schematic diagram of the experimental setup for schlieren imaging of the plasma jet (from Ref. 18).

III. Experimental Approach

A. Design and Operation of the Pulsed Plasma Source

A schematic diagram of the experimental arrangement is shown in Fig. 2. The ET pulsed plasma source design and operation is discussed in detail in Ref. 7; thus, only a brief description is given here. The capillary plasma source is driven by a pulse forming network, consisting of a 251-μF capacitor charged to a maximum of 5.0 kV (3.1 kJ) and a 26-μH inductor. The discharge is initiated by closing an Ignitron switch that connects the capacitor to the capillary electrodes. The capillary is open at one end only and is made of polycarbonate (Lexan, $C_{16}H_{14}O_3$). It is 3 mm in diameter and 30 mm long. To help initiate the discharge, a thin copper fuse wire (64 μm diam) is inserted inside the capillary between the electrodes; it explodes on the closing of the Ignitron. Ablation and ionization of material from the capillary surface then sustains the discharge. The resulting plasma expands rapidly from the open end of the capillary and issues into room air. To reduce erosion, the electrodes were constructed with inserts made of a copper–tungsten alloy (30% Cu, 70% W). The voltage across the capillary was measured as a function of time using a high-voltage probe (Tektronics P6015A). The current was inferred from the voltage output from a Rogowski coil that was magnetically coupled to the current through the major loop of the toroid. The voltage signal induced in the coil is directly proportional to the time rate of change of the total current of the loop. The relative current signal was obtained by integrating the Rogowski coil output with respect to time. The absolute current was obtained by measuring the voltage across the capacitor during the discharge, combined with the relation $i = -C(\mathrm{d}V/\mathrm{d}t)$. The measured voltage and current waveforms were highly repeatable; for example, the peak current was reproducible to within 3%.

B. Emission Spectroscopy Setup

A $\frac{1}{4}$-m spectrometer (Spex 1681C) coupled to an intensified gated 512-element linear array detector (Tracor Northern TN 6143) was used to obtain time-resolved emission spectra from the pulsed plasma jet, as shown in Fig. 2. The spectrometer was calibrated using either an Ne or Hg standard lamp to obtain the absolute wavelength and to measure the instrumental broadening. A tungsten filament standard lamp was used to calibrate the relative spectral response of the entire optical system. The plasma emission was focused by a lens onto an optical fiber that transmitted the light to the spectrometer, and the fiber and lens were coupled together and were micrometer positioned to image different heights along the axis above the exit of the capillary. The spatial resolution along the axis, perpendicular to the line of sight, was found to be 0.86 ± 0.03 mm, as determined by a measurement of the beam waist (FWHM) of an He–Ne laser directed into the opposite end of the fiber and focused by the same imaging lens above the plasma device. The temporal resolution of the spectral measurements was set by a 1-μs gate on the intensifier of the detector array. The temporally and spatially resolved emission spectra were recorded over two wavelength ranges (465–585 and 580–700 nm). Measurements were made at several axial locations along the centerline of the jet and at different times after the initiation of the discharge.

C. Schlieren Imaging Setup

The schlieren technique is a well-established imaging method that enables the visualization of index-of-refraction gradients in a flowfield. As shown in Fig. 3, a pulsed, frequency-doubled Nd:YAG laser was used as the light source. To improve image quality the beam was spatially filtered by passing it through a 25 × microscope objective lens that focused the beam onto a 25-μm pinhole. To avoid burning the pinhole, the laser pulse was first attenuated to about 5 μJ per pulse by reflecting it from three glass flats. The beam was collimated with a parabolic mirror (150-mm diam, f/6) and then focused with an identical mirror onto a knife edge. The beam was then projected onto a ground glass screen ($5.0 \times 5.0 \times 1.6$ mm^3), which was imaged from the "back side" using an ICCD camera (Princeton Instruments ICCD-576, 576 × 384 pixel resolution) fitted with a 105-mm focal length (AF Micro Nikkor) camera lens operated at f/22. To reduce interference from the intense emission from the plasma, the camera was gated to 280 ns, and a laser line filter (532 nm, 3 nm bandwidth) was placed in front of the camera lens. The second schlieren mirror was placed approximately 6 m from the plasma source to reduce further the background luminosity from the plasma.

IV. Results and Discussion

A. Current, Voltage, and Capillary Erosion Measurements

Figure 4 is a plot of the typical voltage and current traces obtained during a discharge with an initial capacitor voltage of 5.0 kV. Figure 4 shows the current, the voltage across the capacitor, and the voltage across the capillary. The error bars represent the precision uncertainty estimated as $\pm 2\delta$, where δ is the standard deviation of a sample of six repeated measurements. The same method will be applied throughout this paper to estimate the precision uncertainties in our measurement, with at least four repeated measurements. The ringing in the capacitor voltage indicates that the system is underdamped, which is typical of these types of discharges because of the low impedance of the plasma.[5] When the discharge is initiated, the voltage across the capillary rapidly increases. If t is the time elapsed

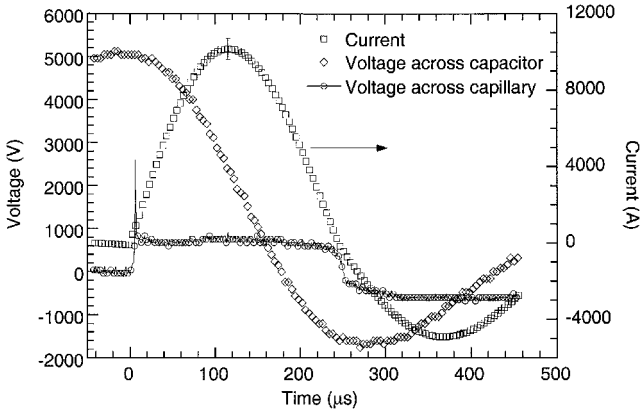

Fig. 4 Typical voltage and current traces obtained during a firing of the plasma jet for an initial capacitor voltage of 5.0 kV.

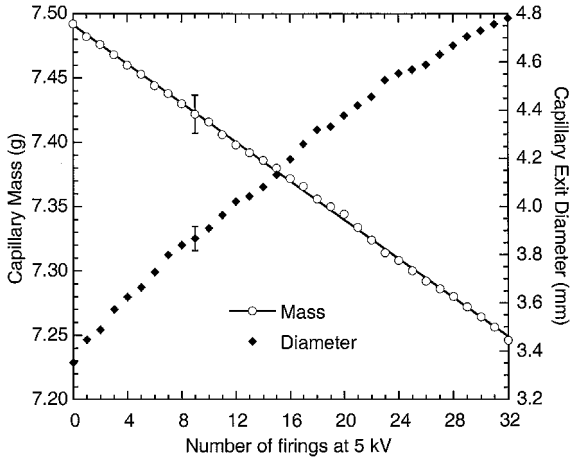

Fig. 5 Capillary mass and exit diameter as a function of the number of repeated firings (from Ref. 18).

from the triggering of the discharge, a peak voltage of 2.6 kV is induced across the capillary over the interval $0 < t \leq 6$ μs, and for $6 < t \leq 240$ μs the voltage is relatively constant at about 0.8 kV. The initial transient voltage spike occurs just before the explosion of the copper wire, and the plasma discharge begins after that, that is, the high discharge current causes the fuse wire to explode about 6 μs after the Ignitron trigger pulse. The peak current of about 10 kA occurs about 115 μs after the start of the discharge. The current reverses direction at about 250 μs, at which time the magnitude of the capillary voltage is significantly reduced and the discharge terminates. The energy dissipated in the plasma can be estimated by the time integral of the product $i(t)V_c(t)$ during the discharge. The energy dissipated is about 1.1 kJ, which is about one-third of the initial stored energy. The balance of the energy is dissipated in the conductors of the pulse-forming network and stored as residual charge in the capacitor.

To see the extent of capillary erosion over a series of shots, the capillary bore exit diameter D and the mass of the capillary were measured as a function of the number of shots. These results are shown in Fig. 5. The uncertainty of the mass of the capillary was estimated to be $\pm 0.2\%$ of the scale. Note that the diameter was measured only at the bore exit, but it is known that the capillary does not erode uniformly, that is, its diameter is not constant along its length. From Fig. 5, it is observed that the exit diameter increases by about 1.3% per shot and that the mass of the capillary decreases approximately linearly with the number of shots. A least-squares fit to the data shows that every firing ablates approximately 7.6 mg of the capillary. A series of preliminary experiments showed that the electron number density n_e in the plasma jet was quite dependent on the capillary bore exit diameter, with larger diameters leading to lower electron number densities. For example, for an initial capacitor voltage of 5 kV, n_e (measured just downstream of the Mach disk) was found to be approximately 1×10^{17} and 1.5×10^{18} cm^{-3} for $D = 5.31$ and 3.81 mm, respectively. To minimize this effect, each capillary was used for a maximum of five shots, corresponding to an increase in diameter of 6.5%.

B. Schlieren Imaging

Figure 6 shows six sequential schlieren images of the expanding plasma jet for an initial voltage of 5 kV (3.1 kJ). The field of view for each image is 132 mm high × 121 mm wide. At about $t = 30$ μs, the blast wave is seen just above the exit of the capillary (between the shadows of two bolt heads). The blast wave development is an unsteady process comparable to the shock propagation from the open end of a shock tube or from the barrel of a rifle.[23] Interestingly, the index of refraction gradients across the blast wave and contact surface are so large that they largely mask the barrel shock inside.

The radius R of the shock, which is assumed to be the distance from the bore exit to the shock measured along the capillary axis, was measured as a function of time t. Note that the position of the shock at a given time is highly reproducible from shot to shot. For example, four schlieren images were taken at time $t = 50$ μs (5-kV initial voltage) and the average value of R was found to be 32.7 mm with a standard deviation of 0.5 mm. Shock trajectory measurements were made for image sequences obtained for initial capacitor voltages of 2.5 (not shown), 3.5 (not shown), and 5 kV (Fig. 6).

The shock trajectory data for all three voltages are shown in Fig. 7. From Fig. 7, it is seen that, for all three cases, the shock radius increases approximately as the first power, that is, linearly, with time.

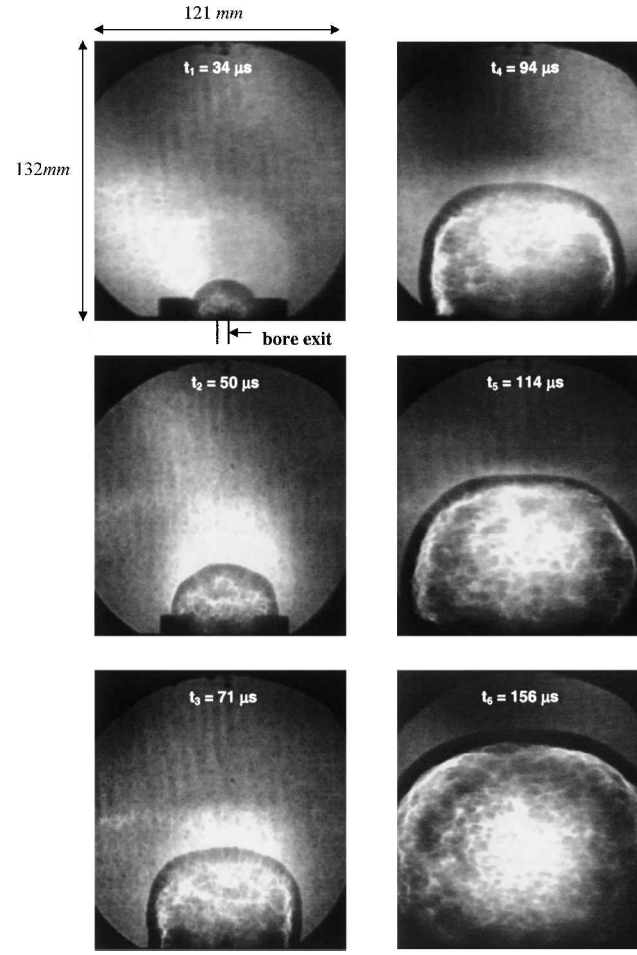

Fig. 6 Schlieren image sequence of the plasma jet for a 5.0 kV discharge; the jet issues between the shadow of two bolt heads seen at the bottom of the image (from Ref. 18).

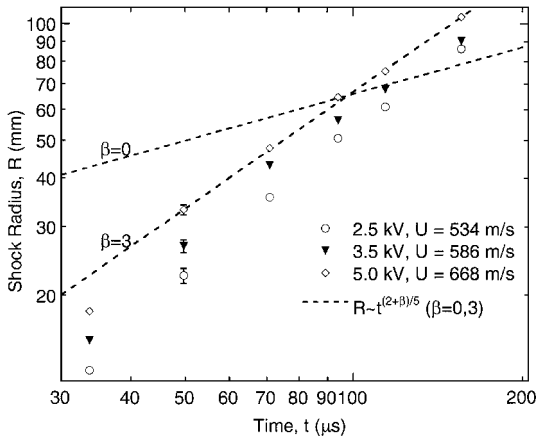

Fig. 7 Time-dependence of the blast wave radius for three different initial energies; the dashed lines are theoretical results corresponding to energy deposition rate parameters $\beta = 0$ and 3 (see text) (from Ref. 18).

The classical solution for the instantaneous deposition of energy at a point leads to the scaling law,[24,25]

$$R(t) \sim (E/\rho_0)^{\frac{1}{5}} t^{\frac{2}{5}} \tag{2}$$

However, studies of muzzle blasts have shown that the blast wave velocities do not necessarily follow this scaling law. Erdos and Del Guidice[26] suggested that a better correlation with experimental data can be achieved by accounting for the continuous, rather than instantaneous, deposition of energy. For the variable energy deposition case, Dabora[27] shows that the equation for blast wave trajectories can be generalized as

$$R(t) \sim (E/\rho_0)^{\frac{1}{5}} t^{(\beta+2)/5} \tag{3}$$

Instantaneous energy deposition corresponds to $\beta = 0$, that is, $R \sim t^{2/5}$. The approximately first-power dependence of R on t observed in Fig. 7 corresponds to $\beta \approx 3$. This value of β indicates a rather gradual rate of energy deposition. Dashed lines corresponding to $\beta = 0$ and 3 are also shown in Fig. 7 for comparison.

From the shock trajectories of Fig. 7, we can infer that the shock velocities are approximately constant with values of 668, 586, and 534 m/s for charging voltages of 5.0, 3.5, and 2.5 kV, respectively. By raising both sides of Eq. (3) to the power $5/(\beta+2)$, and then differentiating with respect to time, we can derive the following scaling law for shock velocity,

$$U = \frac{\mathrm{d}R}{\mathrm{d}t} \sim \frac{(\beta+2)}{5} R^{(\beta-3)/(\beta+2)} \left(\frac{E}{\rho_0}\right)^{1/(\beta+2)} \tag{4}$$

For the case of $\beta = 0$, Eq. (4) gives $U \sim E^{1/2}$ (at constant radius), in agreement with the instantaneous energy deposition model.

A plot of the blast wave velocity vs the initial stored electrical energy E_s is shown in Fig. 8. The solid lines represent shock velocity scalings for different values of β. These results show that the velocity of the blast wave is approximately proportional to $E_s^{1/5}$, corresponding to $\beta = 3$, which is consistent with the finding for shock radius just mentioned.

Trajectories of the measured Mach disk, contact surface, and blast wave locations along the axis of the jet are shown in Fig. 9. The Mach disk and contact surface locations were measured from the visible emission time-sequence images of Kohel et al.[7] Figure 9 also shows that the Mach disk moves away from the bore exit until it attains a maximum standoff at about $t \approx 160$ μs. The direction of the motion is then reversed, and the Mach disk retreats upstream toward the capillary, owing to the decrease of the capillary bore pressure as the discharge terminates. Furthermore, Fig. 9 shows that the blast wave and the contact surface are nearly coincident until about 70 μs, after which a slight separation is observed. We also note that Kim and Wilson[28] developed an analytical model of the unsteady underexpanded jet and found reasonably good agreement with the contact surface trajectories in Fig. 9 if they assumed that $\beta = 2$.

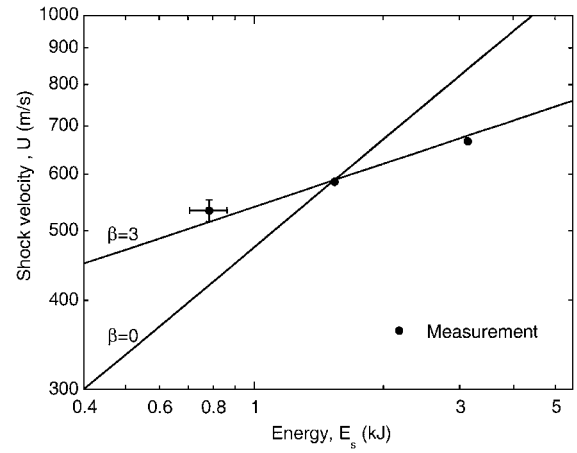

Fig. 8 Dependence of the blast wave velocity on the initial stored electrical energy E_s.

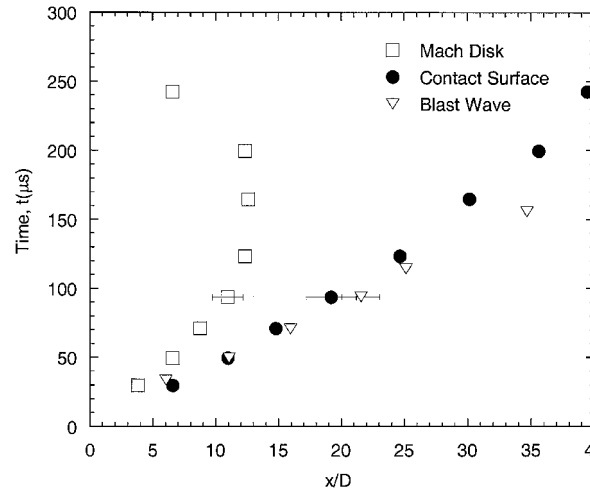

Fig. 9 Experimental axial trajectories of the blast wave, contact surface, and Mach disk; D is the exit diameter of the capillary.

C. General Characteristics of the Plasma Spectra

To investigate the evolution of the excitation temperature and electron density fields within the expanding plasma jet, emission spectra were obtained at several axial positions and times during the discharge. Specifically, emission spectra were acquired at a minimum of seven separate axial locations for 14 different times. It was observed that the measured plasma emission spectra at a particular x and t were highly repeatable from shot to shot. For convenience, we define the nondimensional axial distance, $\zeta_t = x/x_m(t)$, where $x_m(t)$ is the axial distance from the bore exit to the Mach disk at time t, as illustrated in Fig. 1. Three typical axial regions are at the bore exit ($\zeta_t \approx 0$), upstream of the Mach disk ($\zeta_t < 1$), and downstream of the Mach disk ($\zeta_t > 1$). Time-resolved Mach disk locations were obtained from previously obtained emission images[7] and a fit to those data was used to obtain a relationship between Mach disk location and time delay. Figure 10a shows three emission spectra obtained at $t = 90$ μs, but at three different downstream locations ($\zeta_t = 0$, 0.68, and 1.12). Here it is seen that the emission at the exit of the capillary ($\zeta_t = 0$) is predominantly broadband over the spectral range from 580 to 700 nm, and the atomic hydrogen line H_α appears line reversed at 656.3 nm. The broadband emission at the bore exit results from the dense capillary plasma and is consistent with previous measurements made in a similar scale facility.[11,12] For the two locations downstream of the bore exit ($\zeta_t = 0.68$ and 1.12), the broadband emission is substantially weaker, and H_α appears as a distinct emission line and is the predominant feature in the spectral range. The presence of the distinct lines is consistent with the relatively low densities and temperatures that are expected in the interior of an underexpanded jet.

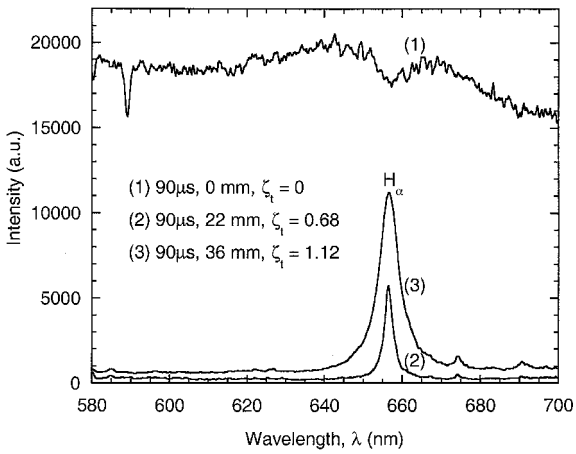

Fig. 10a Temporally and spatially resolved emission spectra obtained at 90 μs after the initiation of the pulsed plasma jet for a 5.0-kV discharge, spectral range 580–700 nm.

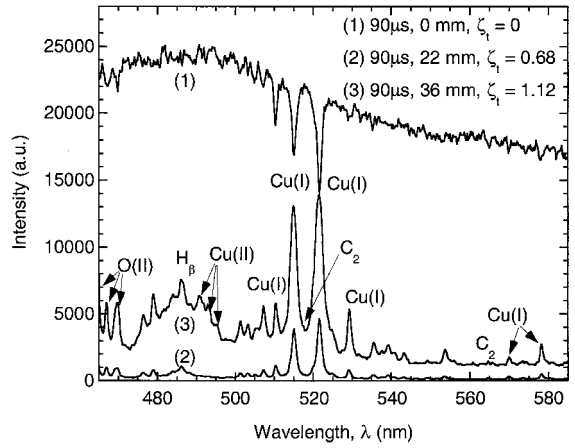

Fig. 10b Same as Fig. 10a for the spectral range 465–585 nm (H_α is the atomic hydrogen emission line at 656.3 nm and I and II indicate neutral and single-ionized atoms, respectively).

Figure 10b shows spectra between 465 and 585 nm, for the same time of $t = 90$ μs and for the three downstream locations of $\zeta_t = 0$, 0.68, and 1.12. Figure 10b shows that, downstream of the bore exit ($\zeta_t > 0$), distinct emission lines are observed for atomic copper [Cu(I)], hydrogen (H_β), copper ions [Cu(II)], and oxygen ions [O(II)]. The emission from Cu arises because it is a constituent of both the electrode material and the fuse wire used to initiate the discharge. H_β(486.1 nm) is also observed in the spectra, but it is too strongly overlapped with adjacent lines to analyze. In addition, the spectra also show evidence of the emission from C_2 (Swan bands). For example, very weak emission features are seen at the wavelengths of the Swan bandheads: 473.7 (1, 0), 516.5 (0, 0), and 563.6 nm (0, 1). The carbon originates from the polycarbonate ($C_{16}H_{14}O_3$) capillary wall, and the C_2 is likely formed at the outer edge of the plasma jet where cooler temperatures enable the recombination of atomic carbon.[11] Figure 10b also shows that the predominately broadband emission at the bore exit ($\zeta_t = 0$) with strong line-reversed features resulting from the self-absorption of copper.

Both Figs. 10a and 10b show that the emission lines downstream of the Mach disk ($\zeta_t > 1$) have higher intensities and larger linewidths than the lines upstream of the Mach disk. This is consistent with the higher densities and temperatures that are expected for compression by a normal shock wave. Axial profiles of the excitation temperature in the plasma jet at different times are shown in Fig. 11. (Although we use the term axial profiles, this is not, strictly speaking, correct because the data are line-of-sight integrated and, therefore, are influenced by the emission from locations that are not on the jet centerline.) The x axis is the nondimensional axial distance ζ_t. The measured excitation temperatures have an estimated uncertainty of ± 2500 K upstream of the Mach disk ($\zeta_t < 1$) and ± 3000 K downstream of the Mach disk ($\zeta_t > 1$), respectively. The uncertainty, which represents the standard error of the excitation temperature, was estimated by means of a first-order fit to data. Figure 11 shows that all of the profiles are approximately similar when plotted as a function of the nondimensional axial distance. This result is interesting because the data represent different times during the discharge where the capillary source conditions would be expected to vary widely. However, regardless of the time (and, hence, the instantaneous current), we observe that two temperatures (upstream and downstream of the Mach disk) can essentially characterize the entire axial profile, that is, $T_{\text{exc}} \approx 12{,}000$ K for $\zeta_t < 1$ and $T_{\text{exc}} \approx 20{,}000$ K for $\zeta_t > 1$. The temperature downstream of the Mach disk should be approximately equal to the temperature at the bore exit. Hankins et al.[11] made bore exit measurements in a similar scale facility and reported temperatures ranging from 14,000 K (1.2 eV) at 1 kJ to 22,000 K (1.9 eV) at 3-kJ discharge energy. We note that our measurements (20,000 K) at 3-kJ discharge energy are in good agreement with their measurements.

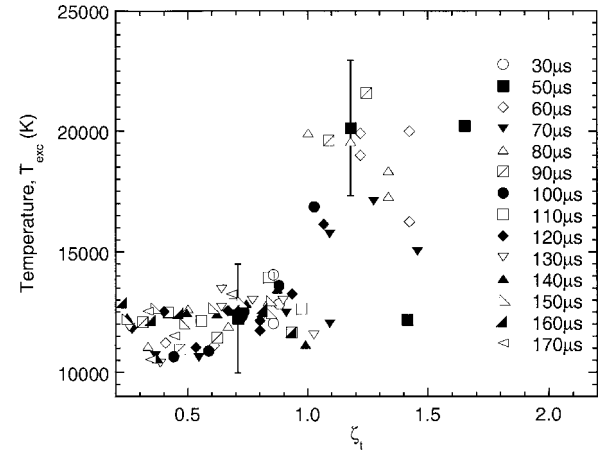

Fig. 11 Variation of the excitation temperature along the axis of the jet for several different times; the downstream coordinate is the nondimensional axial position ζ_t (Ref. 18).

The temperature measurements reported earlier rely on the assumption that the plasma is optically thin at the wavelengths of the copper transitions, that is, there is no absorption of the emitted radiation along the line of sight. The potential for self-absorption was specifically investigated with additional experiments and analysis. Our approach was to make absorption measurements at a single electronic transition of copper and then to assume LTE to infer the absorption that would occur for any other transition along the same path. The line-of-sight laser absorption measurements were performed on the ground state of copper using an Nd:YAG pumped pulsed dye laser tuned to $\lambda = 327.4$ nm ($^2P_{1/2} \leftarrow {}^2S_{1/2}$). Measurements were made at locations just upstream and downstream of the Mach disk ($\zeta_t = 0.8$ and 1.2, respectively). There was no detectable absorption upstream of the Mach disk ($\zeta_t = 0.8$), whereas downstream of the Mach disk ($\zeta_t = 1.2$) the fraction of incident energy absorbed was 40%. We, therefore, will restrict our analysis to the location downstream of the Mach disk because it is here that we expect the greatest self-absorption at the emission lines of interest.

To obtain an order-of-magnitude estimate of the effects of self-absorption, we assume that the optical path in the flowfield is spatially uniform. Then the column density of the ground state of copper $n_o L$ in the optical path can be obtained by using the absorption measurement combined with Beer's law,

$$n_0 L = n_l L = [1/S_{\text{lu}}\phi(\nu)][-\ln \tau(\nu)]$$

Because the transition arises from the ground state, we specifically label the lower state number density, typically denoted by n_l, by n_0. In the preceding expression S_{lu} is given for the optical transition, $\phi(\nu)$ is the line-shape function normalized to unit integral, and $\tau(\nu)$ is the transmissivity at frequency ν. For a transition $l \rightarrow u$ from

lower state l to upper state u centered at wavelength λ, S_{lu} can be calculated from A_{ul}, the corresponding Einstein A coefficient for emission, via

$$S_{lu} = (\lambda^2/8\pi)(g_u/g_l)A_{ul}[1 - \exp(-\Delta\varepsilon_{ul}/kT_{exc})]$$

The term in square brackets is the correction for stimulated emission and is significant at high temperatures. For the $\lambda = 327.4$ nm transition, $\Delta\varepsilon_{ul} = 3.786$ eV, $A_{ul} = 1.37 \times 10^8$ s^{-1}, and $g_u = g_l = 2$, so that at 25,000 K, we have $S_{lu} = 4.84 \times 10^{-7}$ m$^2 \cdot$ Hz. If we assume that the laser is centered on the transition and is narrow relative to the spectral line that is described by a Lorentzian line shape, with a Stark frequency linewidth $\Delta\nu$ half-width at half-maximum (HWHM) of 1.5 THz (corresponding to a Stark linewidth of 1-nm HWHM), then the value of the lineshape function at line center is $\phi(\nu) = 1/(\pi\Delta\nu) = 2.9 \times 10^{-13}$ Hz^{-1}. Substituting these numerical values into the expression for column density, we obtain $n_0 L = 3.7 \times 10^{18}$ m^{-2}.

From the images of the plasma flow, we know that the optical path length in the flowfield is about 40 mm, and so the spatially averaged ground state copper density is $n_0 = 9.2 \times 10^{19}$ m^{-3}, which, as expected, is much less than the electron and ion density ($\sim 10^{24}$ m^{-3}) because Cu, and neutral Cu, in particular, is a trace species in the flow. If we assume thermal equilibrium, we can now calculate the population of the lower states of the Cu transitions and estimate the effects of self-absorption. The absorption cross sections are computed from the Einstein A coefficients as before, and, if we assume the same Stark broadened linewidth for simplicity, we can estimate the transmissivity of the plasma at the peak of the spectral lines. We also note that the effective path length for the emission measurements is actually less than L because the laser beam was propagated across the entire flow, whereas only a small fraction of the emission does so. For this reason, an effective path length, $L_{eff} = L/2$, was used for the self-absorption calculations.

Table 1 shows the spectroscopic constants (see Ref. 29) and the calculated transmission at the center of each spectral line for these conditions ($T = 25{,}000$ K; $L_{eff} = 0.02$ m; and $n_0 = 9.2 \times 10^{19}$ m^{-3}). It can be seen that the transmission is always greater than 85%, corresponding to self-absorption effects of 15% or less. We observe that the ground state does not have the highest population because of the effects of state degeneracy. Additionally, the transitions connecting the highly populated states are not strongly self-absorbed because these are forbidden transitions with small Einstein A coefficients and correspondingly small absorption cross sections.

Also note that the emission transitions with the strongest self-absorption effects arise from states with intermediate energy (6.2 eV). Thus, self-absorption will have relatively little effect on the slope of the line in a Boltzmann plot and, thus, will have relatively little effect on the temperature determined. Although the preceding analysis is based on a spatially averaged approximation, it can be seen that the effects of self-absorption are likely to be small and well within the experimental uncertainty, except for the region very close to the capillary exit.

D. Electron Density

To determine the electron number densities, we used the results of Gigosos and Cardenoso,[30] who calculated the Stark widths of the first three lines of the Lyman and Balmer series of hydrogen, including the important contribution of ion broadening. Their simulation results show that the Stark widths do not have a strong dependence on either the plasma excitation temperature, nor on atom–ion reduced mass μ. To obtain electron number densities, we used the linewidth of H_α and took the plasma temperature to be 15,000 K and the reduced mass to be 1.0 amu (Ref. 30) (roughly corresponding to a hydrogen emitter in a mixture of heavier ion perturbers).

Figure 12 (see Refs. 31 and 32) shows measured electron number density n_e profiles along the axis of the plasma jet at several times. The measurements have an estimated uncertainty of 4.1×10^{16} cm^{-3} for $\zeta_t < 1$ and 4.9×10^{17} cm^{-3} for $\zeta_t > 1$, respectively. In this case, as with the temperature data, the profiles are seen to be very similar. Upstream of the Mach disk, the density is relatively constant and then undergoes an abrupt jump across the Mach disk ($\zeta_t = 1$). The measured electron number densities range from 1.7×10^{17}–5.5×10^{17} cm^{-3} upstream of the Mach disk to 10^{18}–2.5×10^{18} cm^{-3} downstream of the Mach disk. Furthermore, despite significant scatter in the measurements, there appears to be a trend toward lower electron densities further downstream of the Mach disk, which should be consistent with the decreasing temperatures downstream of the Mach disk hinted at in Fig. 12.

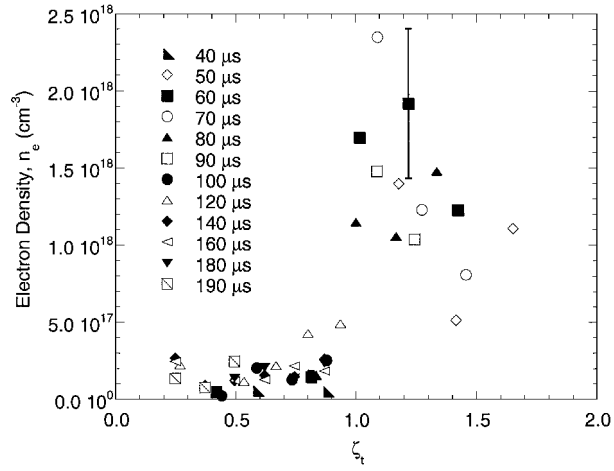

Fig. 12 Variation of electron number density along the axis of the jet for several different times (from Ref. 31).

Hankins and Mann[12] showed that the electron densities obtained at the exit of an ET source of similar scale to ours varied from 7.6×10^{17} cm^{-3} at 1-kJ to 2.0×10^{18} cm^{-3} at 5-kJ discharge energy. (At 3-kJ discharge energy, the density of $\approx 1.6 \times 10^{18}$ cm^{-3} can be deduced from their data.) We note that our measurements for electron densities in the regions downstream of Mach disk ($\zeta_t > 1$) show an excellent agreement with their measurements.

V. Conclusions

In this study, we have made temporally and spatially resolved emission spectroscopic measurements and conducted schlieren visualization of a pulsed plasma jet produced by an ET capillary discharge issuing into room air. Temperature and electron number density axial profiles were obtained at several times throughout the discharge at an energy of 3.1 kJ. Results show that the plasma temperature and electron density jump across the Mach disk, as expected. Regardless of the time within the discharge, the temperatures are approximately 20,000 K and 12,000 K downstream and upstream of the Mach disk, respectively; the corresponding electron densities are $\geq 1.0 \times 10^{18}$ and $\approx 2.5 \times 10^{17}$ cm^{-3}, respectively. In addition, we have measured the trajectory of the blast wave using the schlieren imaging technique at discharge energies of 0.78, 1.5, and 3.1 kJ. The results were compared to previous results for the contact surface and Mach disk and show that the blast wave and contact surface are nearly coincident until about 70 μs after the plasma initiation. Approximately 160 μs after plasma initiation, the supersonic expansion has grown to its maximum downrange extension, and the barrel shock structure is fully established. At later times, the blast wave decouples from the driving core jet flow, and the barrel shock retreats toward the capillary exit. Furthermore, the analysis of the blast wave trajectories shows that the scalings of the shock radius with time and of the shock velocity with energy are consistent with a model that accounts for the continuous deposition of energy at a point.

Acknowledgments

This study was supported by the Institute for Advanced Technology at the University of Texas at Austin. Permission to publish Figs. 1, 3, 5, 6, 7, and 11 was granted by the Korean Society of Mechanical Engineers (Copyright 2000), and permission to publish Fig. 12 was granted by the American Institute of Physics (Copyright 2000). Some of these results were previously published

in Ref. 18 without the knowledge of the senior authors (Clemens and Varghese), and, therefore, this paper, rather than Ref. 18, should be considered the primary reference for this work.

References

[1]Hewkin, D., and Figura, E., "Fundamental Research and Numerical Modeling of the Internal Ballistics of Electrothermal Chemical Guns," *IEEE Transactions on Magnetics*, Vol. 29, No. 1, 1993, pp. 561–566.

[2]Greig, J. R., Earnhart, J. R., Winsor, N., McElroy, H. A., Juhasz, A. A., Wren, G. P., and Morrison, W. F., "Investigation of Plasma Augmented Solid Propellant Interior Ballistic Processes," *IEEE Transactions on Magnetics*, Vol. 29, No. 1, 1993, pp. 555–560.

[3]Woodley, C. R., "A Parametric Study for an Electrothermal-Chemical Artillery Weapon," *IEEE Transactions on Magnetics*, Vol. 29, No. 1, 1993, pp. 625–630.

[4]Kaplan, Z., Saphier, D., Melnik, D., Gorelic, Z., Ashkenazy, J., Sudai, M., Kimhe, D., Melnik, M., Smith, S., and Juhasz, A., "Electrothermal Augmentation of a Solid Propellant Launcher," *IEEE Transactions on Magnetics*, Vol. 29, No. 1, 1993, pp. 573–578.

[5]Burton, R. L., and Turchi, P. J., "Pulsed Plasma Thruster," *Journal of Propulsion and Power*, Vol. 14, No. 5, 1998, pp. 716–735.

[6]White, K. J., Katulka, G. L., Khong, T., and Nekula, K., "Plasma Characterization for Electrothermal-Chemical (ETC) Gun Applications," U.S. Army Research Lab., Rept. ARL-TR-1491, Aberdeen Proving Ground, MD, 1997.

[7]Kohel, J. M., Su, L. K., Clemens, N. T., and Varghese, P. L., "Emission Spectroscopic Measurements and Analysis of a Pulsed Plasma Jet," *IEEE Transactions on Magnetics*, Vol. 35, No. 1, 1999, pp. 201–206.

[8]Nusca, M. J., White, K. J., Williams, A. W., Landsberg, A. M., Young, T. R., and Lind, C. A., "Computational and Experimental Investigations of Open-Air Plasma Discharges," AIAA Paper 99-0865, Jan. 1999.

[9]Beyer, R. A., and Bunte, S. W., "Spatial and Temporal Studies of Electrothermal Chemical (ETC) Plasmas," U.S. Army Ballistic Research Lab., TR BRL-TR-3324, Aberdeen Proving Ground, MD, 1992.

[10]Mach, H., Werner, U., Masur, H., and Steinbach, C., "Spectroskopische Untersuchungen in der Expansionskammer eines Electrothennischen Beschleunigers," Deutsch–Franzoesisches Forschungsinstitut Saint-Louis, Rept. 103/94, Weil-am-Rhein, Germany, Nov. 1994.

[11]Hankins, O. E., Bourham, M. A., Earnhart, J., and Gilligan, J. G., "Visible Light Emission Measurements from a Dense Electrothermal Launcher Plasma," *IEEE Transactions on Magnetics*, Vol. 29, No. 1, 1993, pp. 1158–1161.

[12]Hankins, O. E., and Mann, D., "Analyses of Molecular and Neutral Atomic Emission Spectra from an Electrothermal Launcher Plasma," *IEEE Transactions on Magnetics*. Vol. 31, No. 1, 1995, pp. 410–413.

[13]Lochte-Holtgreven, W., *Plasma Diagnostics*, edited by W. Lochte-Holtgreven, Wiley, New York, 1968, pp. 178–183.

[14]Wiese, W. L., "Line Broadening," *Plasma Diagnostic Techniques*, edited by R. H. Huddlestone and S. L. Leonard, Academic Press, New York, 1965, pp. 265–317.

[15]Griem, H. R., *Spectral Line Broadening by Plasmas*, Academic Press, New York, 1974, pp. 303–307 .

[16]Oza, D. H., Greene, R. L., and Kelleher, D. E., "Collisional Broadening of the Balmer-α Transition of H and H^+ in Plasmas," *Physical Review A*, Vol. 37, No. 2, 1988, pp. 531–536.

[17]Oza, D. H., Greene, R. L., and Kelleher, D. E., "Dependence of the Half Widths of Plasma-Broadened Hydrogen Lines on Reduced Mass, Temperature, and Density," *Physical Review A*, Vol. 38, No. 5, 1988, pp. 2544–2551.

[18]Kim, J. U., and Kim, Y. J., "Investigation on the Flow Field Characteristics of a Highly Underexpanded Pulsed Plasma Jet," *KSME International Journal*, Vol. 15, No. 12, 2001, pp. 1691–1698.

[19]Thompson, P. A., *Compressible-Fluid Dynamics*, McGraw–Hill, New York, 1972, pp. 462–464.

[20]Crist, S., Sherman, P. M., and Glass, D. R., "Study of the Highly Underexpanded Sonic Jet," *AIAA Journal*, Vol. 4, No. 1, 1966, pp. 68–71.

[21]Abbett, M., "Mach Disk in Underexpanded Exhaust Plumes," *AIAA Journal*, Vol. 9, No. 3, 1971, pp. 512–514.

[22]Eggins, P. L., and Jackson, D. A., "Laser Doppler Velocity Measurements in an Under-Expanded Free Jet," *Journal of Physics D: Applied Physics*, Vol. 7, No. 14, 1974, pp. 1894–1906.

[23]Klingenberg, G., and Heimerl, J. M., "Gun Muzzle Blast and Flash," Vol. 139, *Progress in Astronautics and Aeronautics*, AIAA, Washington, DC, 1992.

[24]Taylor, G. I., "The Formation of a Blast Wave by a Very Intense Explosion," *Proceedings of the Royal Society of London, Series A: Mathematical and Physical Sciences*, Vol. A201, 1950, pp. 159–174.

[25]Sakurai, A., "A Blast Wave Theory," *Basic Developments in Fluid Dynamics*, edited by M. Holt, Vol. 1, Academic Press, New York, 1964, pp. 309–375.

[26]Erdos, J. I., and Del Guidice, P. D., "Calculation of Muzzle Blast Flowfield," *AIAA Journal*, Vol. 13, No. 8, 1975, pp. 1048–1055.

[27]Dabora, E. K., "Variable Energy Blast Waves," *AIAA Journal*, Vol. 10, No. 10, 1972, pp. 1384–1386.

[28]Kim, K., and Wilson, D. E., "Theoretical Analysis of a Plasma Jet Impingement on a Nonreacting Surface," AIAA Paper 99-0455, Jan. 1999.

[29]*CRC Handbook of Chemistry and Physics*, 76th ed., edited by David R. Lide, CRC Press, Boca Raton, FL, 1996, pp. 10–142.

[30]Gigosos, M. A., and Cardenoso, V., "New Plasma Diagnosis Tables of Hydrogen Stark Broadening Including Ion Dynamics," *Journal of Physics B: Atomic and Molecular Physics*, Vol. 29, No. 2, 1996, pp. 4795–4838.

[31]Kim, J. U., Clemens, N. T., and Varghese, P. L., "Characterization of a High-Density Plasma Produced by Electrothermal Capillary Discharge," *Applied Physics Letters*, Vol. 80, No. 3, 2002, pp. 368–370 (see Ref. 32 for corrected author list).

[32]Kim, J. U., Clemens, N. T., and Varghese, P. L., "Characterization of a High-Density Plasma Produced by Electrothermal Capillary Discharge," *Applied Physics Letters*, Vol. 80, No. 15, 2002, p. 2806 (Erratum).